

Detection of a transiting Hot Jupiter around WASP-44

Adriana Barbieri

Alessandro Bianchetti

January 6, 2022

Abstract

In the following report we work on WASP-44 b, an exoplanet orbiting around its G-type parent star, located in the constellation of Cetus. We first examine its atmospheric parameters and derive its mass and radius (Morton 2015). Then, we correct for limb darkening effect through different methods (Claret et al. 2011, Claret 2017, Claret 2018). We also take some images obtained with Copernico telescope at the Asiago Observatory into consideration and, after proper correction, we use them to extract the light curve of the alleged planet.

1 Introduction

Confirmed exoplanets are growing in number year by year, and transit method is nowadays a widespread and hugely successful detection method. Most planets indeed are by now discovered by tracing the lightcurve and searching for any sign of a weakening in the flux.

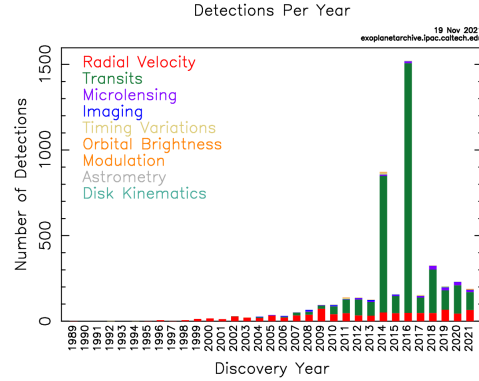


Figure 1: Confirmed exoplanets distribution per year of detection via different methods. Credits to <https://exoplanetarchive.ipac.caltech.edu/>

In this report we focus on WASP-44 b, a Jupiter-size planet orbiting around a G-type star, located in the constellation of Cetus. Among the numerous available reports on the planet, we decided to make a conservative choice and avoid any result which is not inferred via spectroscopy. This leads us to rule out several papers regarding our target of interest and exclusively work with the discovery paper (Anderson et al. 2011). In this paper, estimates of the atmospheric parameters of WASP-44 are provided via an analysis of the width of the spectral lines.

2 The transit method

The transit method is a photometric indirect method of detection of exoplanets, which consists in the observation of a drop in the flux of

a star due to the transit of a planet across the stellar disk.

The subsequent variation of the measured stellar luminosity is proportional to the ratio of the projected areas of the planet and the star, or equivalently, the dimming of the flux is proportional to the ratio of the square of the respective radii; therefore, known the radius of the star from its spectrum, the radius of the planet can be easily obtained from the measured depth of the flux.

Moreover, if combined with radial velocities measurements, this method allows to compute also the average density of the exoplanet.

It is important however to notice that limb darkening, stellar activity and atmospheric effects may pollute the observational transit curve and must be all taken into account.

The modelled transit light curve is distinguished by a characteristic trapezoidal shape, whose main geometrical parameters are the impact parameter, the ingress/egress and transit duration, and the transit depth.

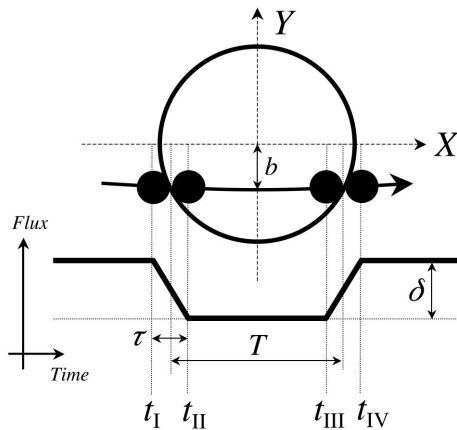


Figure 2: Simplified transit light curve. Credits to Winn [2010]

The geometry of the system places a strong constraint on the inclination of the orbital plane of the planet with respect to the line of sight: the transit can be observed exclu-

sively for almost edge-on orbits, meaning orbital planes that are as parallel as possible to the line of sight. This condition yealds a low probability of detection, which in turn requires a huge number of target stars to carry on successfull observations.

Furthermore, at least two transits are required to determine the orbital period of the extrasolar planet candidate, and since the duration of the transit is very short compared to the orbital period, continuous and prolonged observations are required in order to detect it.

It is of capital importance to be aware of the selection biases that are intrinsic to this method (and to the current available technology): indeed it yealds the largest detection probability for large massive planets orbiting very close to small and quiet stars, thus selecting Hot Jupiters around late type stars as ideal targets.

3 Data analysis

3.1 Inferring mass and radius

The H_α line was used to determine the effective temperature (T_{eff}), while the NaI D and MgI b lines were used as surface gravity ($\log g^*$) diagnostics (Anderson et al. 2011). The elemental abundances, including $[Fe/H]$ were determined from equivalent width measurements of several clean and unblended lines. This led to proper estimation of the atmospheric parameter triplet T_{eff} , $\log g^*$ and $[Fe/H]$. Quoted errors include statistical uncertainties only. In the same conservative spirit we previously showed, we add in quadrature a further term to the errors of all three parameters (Sousa et al. 2011). We are in fact more interested in an accurate result rather than in a precise one. This leads to the following results

T_{eff} (K)	$\log g^*$	$[Fe/H]$
5400 ± 162	4.5 ± 0.2	0.06 ± 0.11

3.2 Limb darkening correction

Limb darkening is an important effect that cannot be neglected when observing a star. In short, the edges of the luminosity profile of a star always look darker than the core: this occurs because there is a physical, constant distance L at which the optical depth is equal to unity, further than which the observations are not possible since photons are completely absorbed and do not reach the observer. This characteristic size, however, can extend deep inside the hot layers of the star if we look straight to the center, being L radial, while it can stop at the colder, outer layers if we look at the edges of the star, since L and our line of sight (LoS) are not radial anymore.

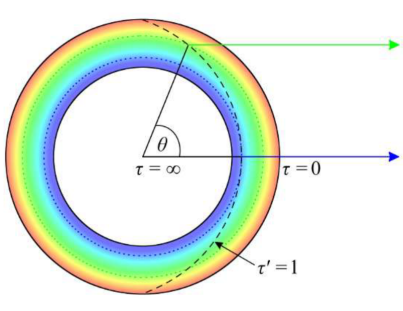


Figure 3: Limb darkening effect scheme. Credits to <https://ediss.sub.uni-hamburg.de>

Correcting for this effect may be challenging. Indeed we can measure it directly only for the Sun, while we need to model it somehow for any other star, thus figuring out a proper law for the intensity decrease $I(\mu)$, where $\mu = \sqrt{1 - r^2}$. Many choices are plausible at this point: a uniform behaviour, a linear, a quadratic, a square-root or a logarithmic law are all valid guesses. Parametrizing such laws introduces the so-called *LD-coefficients*, which will depend on the stellar parameters. Knowing the latter relationship (for instance calibrating it based on a large sample of stars) allows to obtain the coefficients directly from

the atmospheric parameters. The alternative way is fitting the light curve leaving the coefficients as free parameters.

The choice of the functional dependence on μ is a delicate one. Multiple approaches can be followed, basing on different papers. This analysis is addressed in A.

3.3 Bias and flat field correction

CCDs (Charged Coupled Devices) are the privileged detectors for photon counting, due to their high quantum efficiency. The images produced are *raw* and must be properly *pre-reduced* before being analysed. Pre-reduction goes through different steps:

- **bias** is the individual pixel-to-pixel offset level, and it is a zero-exposure instrumental factor, thus it is always an added contribution to any signal. Therefore it must be removed in order to isolate the photons of astrophysical origin. The root mean square of the bias corresponds to the so-called *readout noise*. We perform an average across all the pixels to get an estimate of the bias;
- a **flat field** is a calibration image obtained by illuminating homogeneously the pupil of the telescope, using twilight sky or appropriate, back-lighted screens. This correction factor is to be applied on each pixel and then also normalised, after the overall bias correction;
- **differential photometry** is a great way to keep track of any noise variation. The idea is to take a reference star close enough to the target: any environmental or instrumental variation will affect both sources. Working with flux ratios will make only astrophysical variations evident!

For pre-reductions steps, we use the code *huggy*. We first perform bias correction, than the flat field correction. The corrected images are ready for aperture synthesis.

3.3.1 Bias correction

We run *huggy-bias.e* inputting the raw images.

```
huggy-bias.e A*.fits
```

Many bias images are produced, displaying the zero offset of the pixel board. *Master bias* is the average of all these files. Plotting the intensities of the offset level of the pixels yields a concrete view of the correction.

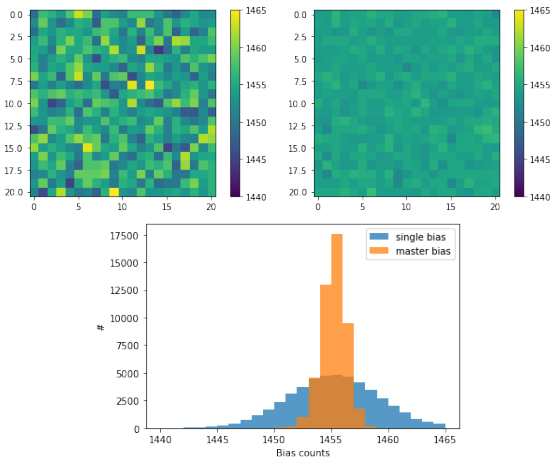


Figure 4: Comparison between random bias frame and master bias

Note that the master bias frame distribution is peaked and much closer to a unique constant value, as all pixels behaved in the same way, like in an ideal situation. We can see this even numerically, by looking at the dispersions of the above distributions: $\sigma_{rb} = 3.82$ and $\sigma_{mb} = 0.89$.

3.3.2 Flat field correction

We now run *huggy-flat.e* inputting a normalization fraction, meaning the fraction of pixels

we want to account for, ruling out the sides which are often polluted by overscan columns. These are visible in the form of dark stripes on the sides of any flat field take. Then we have to input the overscan values, usually set to 0. Subsequently, we need to provide the master bias file, which will be subtracted from the data. Finally, we input all the available flat fields.

```
huggy-flat.e 0.9 0 0 mb.fits A*.fits
```

This will produce an output file showing the average response of pixels to an external light source. Minor differences in such response are important and must be accounted for.

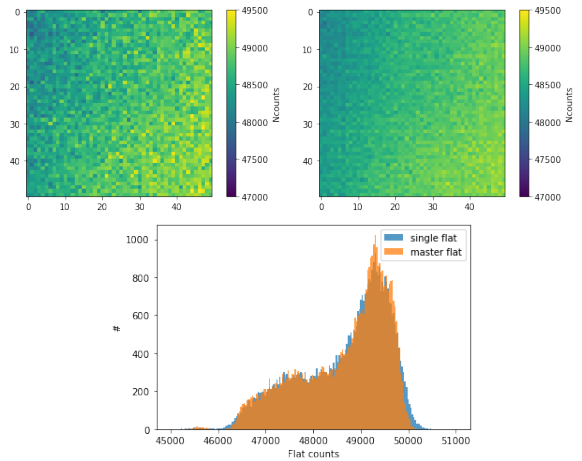


Figure 5: Comparison between random flat field and master flat

3.4 Final correction

The final step is applying the correction files obtained in the previous parts.

```
huggy-correct.e mb.fits mfn.fits A*.fits
```

The final correction code requires the master bias and the normalised master flat, and of course all the target images, that are all going to be corrected.

3.5 Extracting the light curve

We are approaching the very heart of this analysis, preparing for aperture synthesis. We now need to display the science images, make sure to identify the correct target and select a proper background analysis around it. To do that, we have to properly circle the source and create a slightly larger circle around it (*ds9* was the used tool). The same procedure must be repeated (with the same inner and outer radii) on a properly selected reference star, close to and roughly as bright as the target. We hereby report the coordinates of the target and of the chosen reference star, in pixel units.

	x_c	y_c
Target	170	37
Reference	288	57

$$R_{in} = 11, R_{out} = 20$$

Now we need to call *huggy-psf.e* and input the coordinates of the center of the target, the inner and outer radii, and a random corrected image.

```
huggy-psf.e x0 y0 Rin Rout A*.fits
```

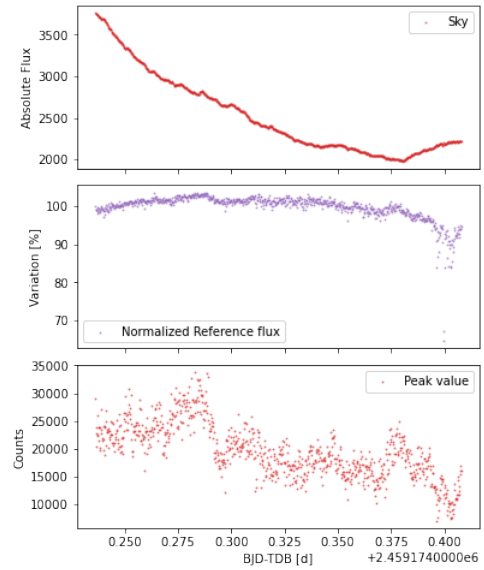
This yields information about the Point Spread Function, meaning how the the flux is distributed as a function of the distance from the core of the source. The output displays the radii at which we find 90, 95 and 99% of the total flux. We take note of this output.

Photometry analysis is carried out by *sentinel.e*, which needs the coordinates of the target and of the reference stars, followed by the radii of two selected apertures from the previous output. Also, we need again inner and outer radii of the selected region for the analysis, as well as the full-corrected images of the target.

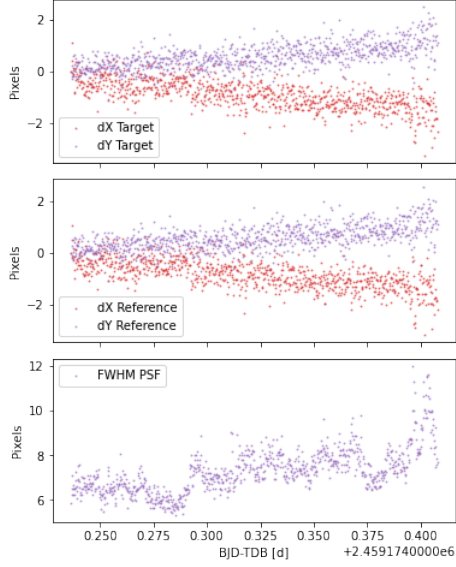
```
sentinel.e x0 y0 xr yr a1 a2 Rin Rout c
A*.corr.fits
```

where $c = \{1, 2\}$ selects the centroiding method (gaussian/moment). For a relatively faint star like ours ($J \approx 11$) our choices are $a_1 = 4.71$ and $a_2 = 5.97$, corresponding to 90 and 95%.

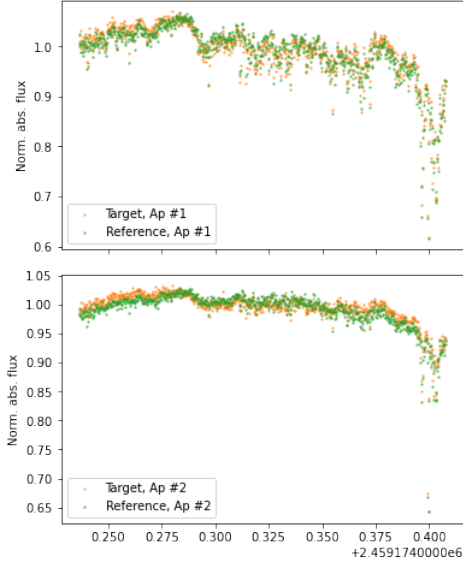
The *sentinel* output is the starting point for TASTE analysis. This file contains the main information about the target and the sky, keeping track of the respective photometries. In fact, let's start by checking the evolution of the sky background throughout the observation session, and also to the behaviour of the reference star.



The sky flux has been constantly decreasing in time, so we expect less and less disturbance as the observation proceeds. The reference star, on the other hand seems to be pretty stable in terms of flux. We also want to make sure that reference stars are correctly comoving: to do that, we plot the variation in position at every time step and check we have similar motion.

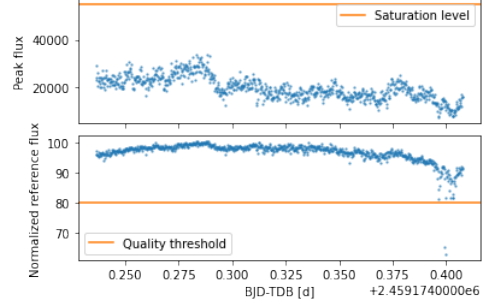


Next, we compare the flux plot with the two different aperture we have chosen.



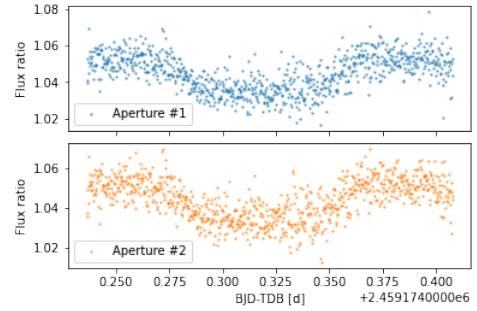
The second case (95%) seems to be slightly less noisy: that's our first clue that this aperture might be the best suited choice for the aperture analysis.

As a further goodness check, one may take a look at the peak value trend of the target source and compare it to the saturation level.



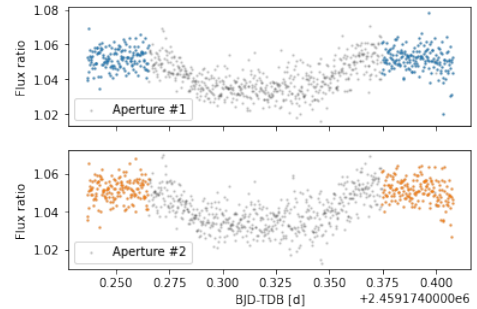
The peak value is well below the saturation limit, and we also see that the quality factor is above the required threshold.

We can finally visualise the transit, with both apertures.

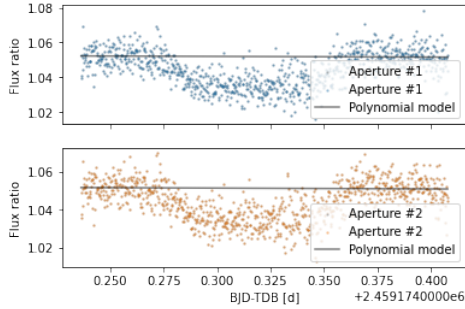


We still see that the wider aperture seems to have less dispersion than the other case, and we keep that in mind.

In order to evaluate the depth of the transit, we need to identify the "height" of the continuous level: to do that, we need to exclude the transit datapoints and try out a polynomial fit, hoping to find a perfectly horizontal line. That will be our reference for the stellar flux.



To perform the fit, we ruled out all the points during the transit by roughly selecting an ingress and egress time. A quadratic law ($p_0x^2 + p_1x + p_2$) was chosen to set things up in the most general case. A least square fitting via numpy function *np.polyfit* yields the following results:



# ap	$p_0(\cdot 10^{-10})$	$p_1(\cdot 10^{-7})$	$p_2(\cdot 10^3)$
1	-7.98	1.43	4.82
2	-8.98	1.42	5.43

We immediately notice that both p_0 and p_1 are well compatible with zero, meaning that only a constant term survives: that represents the level of the continuous, with respect to which we're going to compute the depth of the transit.

4 Conclusions

A Limb darkening analysis

A.1 Claret 2017

We can represent data tables in Claret 2017 as 2D histograms, after proper unfolding of the data tables attached to the paper. To do that, we first fix metallicity, then gravity and see how the corresponding LD coefficients c_1 and c_2 depend on all three atmospheric parameters.

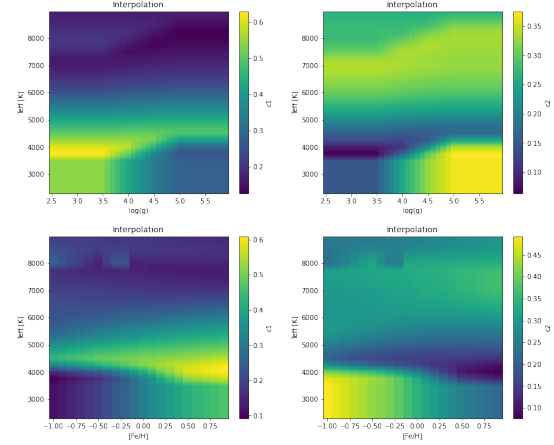


Figure 6: LD coefficient with fixed metallicity, fixed gravity

Furthermore, it's very interesting to check the strength of the dependance on each atmospheric parameters. Turns out LD coefficients are essentially a function of temperature, and minor dependences on gravity and metallicity can be barely appreciated.

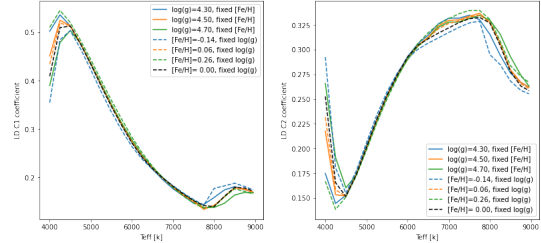


Figure 7: LD coefficient as a function of atmospheric parameters

A relevant dependance on gravity and metallicity can only be noticed at high temperatures, where we should carefully select the proper curve. But in the range we're interested in ($\approx 5400K$) the curve is degenerate and the choice of these parameters is secondary.

We perform a Montecarlo simulation, generating 1000 random atmospheric parameters around the actual ones. Even in this case we see that the distribution of the fixed-metallicity estimates is almost overlapping with the fixed-

gravity one, thus confirming c_1 and c_2 not very sensitive on metallicity and gravity.

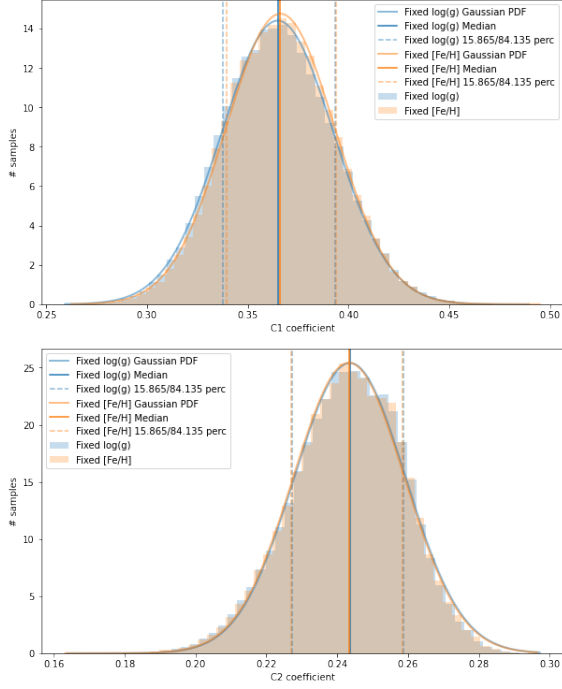


Figure 8: Montecarlo simulation for c_1 and c_2 , for fixed metallicity and for fixed gravity

The two estimates are well compatible, thus authorizing a weighted average: $c_1 = 0.366 \pm 0.019$ and $c_2 = 0.243 \pm 0.011$.

Another way to deal with the same table is by selecting from the set two values of metallicity or gravity, an upper and lower limit, instead of just one reference value. This way we build two matrices and interpolate between the two to get to the desired result. The rest of the procedure is the same as just explained, leading to other estimate of the LD coefficients.

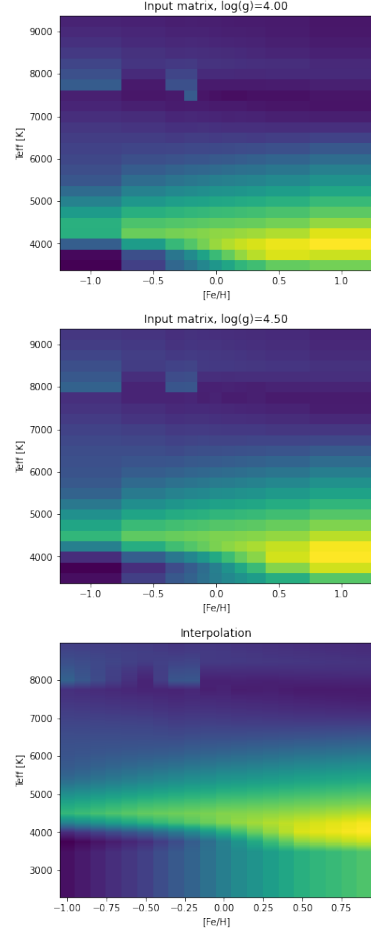


Figure 9: Matrices obtained by fixing gravity to $\log g = 4.0$ to 4.5 , plus the interpolated matrix

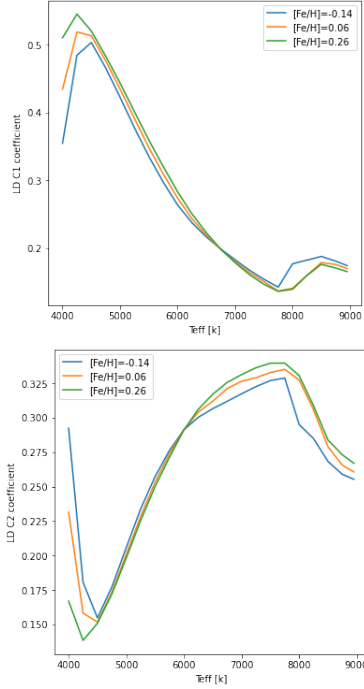


Figure 10: LD coefficients trend in the $T_{eff} - [Fe/H]$ plane

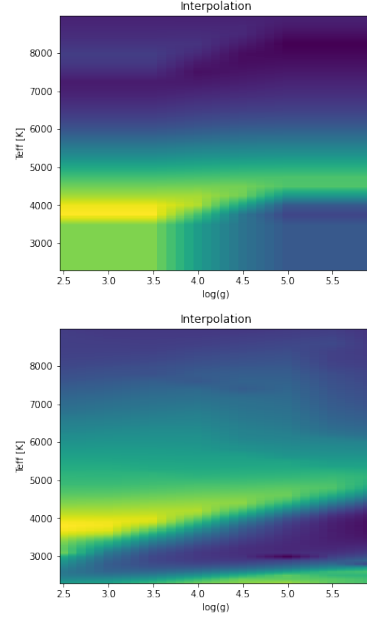


Figure 11: Final, interpolated matrices for the two methods (2017 left, 2018 right)

This can be done in the same exact way by fixing metallicity instead.

A.2 Claret 2018

A successive paper provided a new method to model the LD coefficients dependency on atmospheric parameters. We'd like to check if this leads to different results with respect to the 2017 paper. Unfolding the table requires the same procedure we've already described. Just note that in both cases we fix metallicity, and for the 2018 table metallicity must be fixed to 0, since the method is conceived for zero-metallicity stars.

And finally we can display the dependency of the LD coefficients for the two-parameters game.

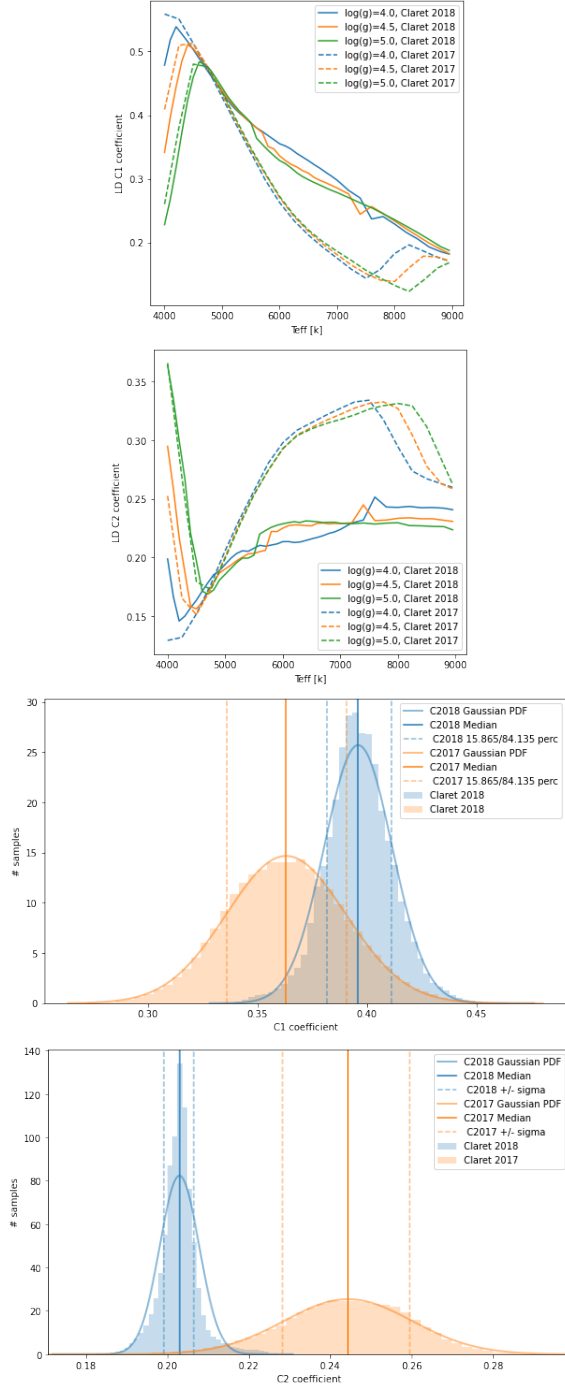


Figure 12: c_1 and c_2 trend, and comparison between the final results

See how there is an actual difference be-

tween the adopted methods, that lead in fact to slightly different results for the LD coefficients. The good news is, they're largely compatible: see how each value is within a few errorbars away from the other.

A.3 Claret 2011

We use another table from an older paper by the same author, where even filters have a role. By looking at the header of our dataset, we find the right filter to be r^* (SDSS). Remember that transits look differently when observed through different filters, and also that boxier transits make ingress/egress time determination easier. The unfolding technique is always the same. This time, we account for stellar models (ATLAS/PHOENIX) and interpolation technique (least squares/flux conservation), for a grand total of 4 combinations. These are the very final results.

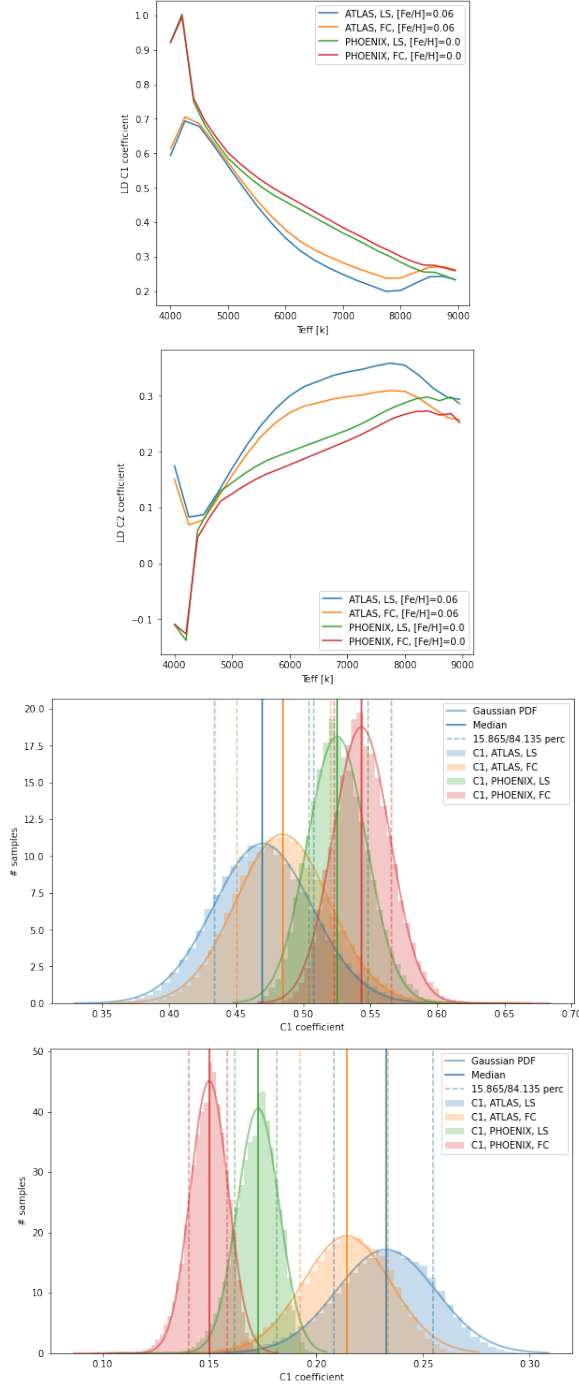


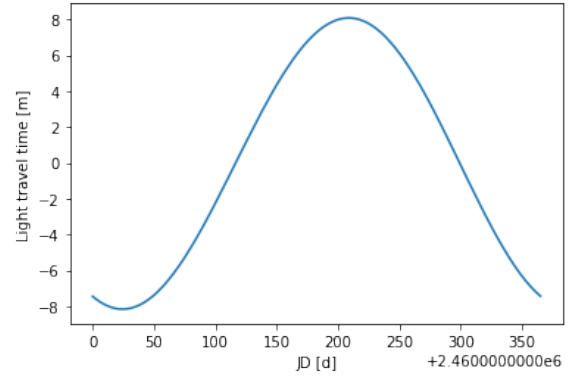
Figure 13: c_1 and c_2 trend, and comparison between the final results

Again, all results are fully compatible.

B Time correction

When dealing with *sentinel.dat* output, we need to properly convert the time series, contained in columns two of the datatable. To do that, first we convert from minutes to days, then add the zero-point in Julian Date format, and finally also add half exposure time (after proper conversion in days).

Moreover, we can make use of the *Time* method to keep count of the time taken by the light to travel from the source position to the location of the observatory (Cima Ekar, Asiago). Since the Earth is in motion, light time travel is variable and follows a sinusoidal behaviour.



References

- Morton, Timothy D. (2015). eprint: 1503.010
- Claret, A. et al. (2011). *A&A* **529**, A75
- Claret, A. (2017). *A&A* **600**, A30
- Claret, A. (2018). *A&A* **618**, A20
- Anderson, D.R. et al. (2011). *MNRAS* **422**
- Sousa, S.G. et al. (2011). *A&A* **533**, A141